

# **Dislocation nucleation and propagation in the vicinity of a crack tip: some limiting case results**

Pablo D. Zavattieri<sup>1</sup>, Louis G. Hector Jr<sup>1</sup>, Jean Gullickson<sup>2</sup>, Alan Needleman<sup>2</sup>

<sup>1</sup>General Motors Research and Development Center, Warren, MI 48090

<sup>2</sup>Division of Engineering, Brown University, Providence, RI 02912

## **ABSTRACT**

In the present work, the discrete dislocation and cohesive zone models are combined to analyze small scale yielding around a crack tip under mode I loading conditions. The crack tip is prevented from growing (although it is allowed to open) through application of a suitably high value of the peak opening stress. The peak stress and corresponding normal separation are specified by a cohesive zone law that governs decohesion ahead of the crack tip. Plastic deformation is limited to a small process window that surrounds the stationary crack tip. We specifically examined some limiting case solutions for extreme obstacle densities and slip plane spacings within the small strain, discrete dislocation framework: these solutions have not previously been investigated to sufficient detail. We examined materials that are representative of face-centered cubic (FCC) and body-centered cubic (BCC) materials from the standpoint that they capture only two-dimensional stress states in what are otherwise three-dimensional stress states in real materials. The ultimate goal of this work is to generate cohesive zone laws that contain information from multiple length scales to model failure processes involving interfacial separation (e.g. coating delamination, intergranular and transgranular fracture, debonding of hard particles, etc.). This work was conducted as part of the GM/Brown Collaborative Lab. R&D report# 9649, Aug. 2003

## Introduction

The mechanisms of interfacial separation are complicated. These mechanisms involve, among other things, the breaking of bonds at the atomic scale and the nucleation, propagation, and interaction of dislocations with themselves and with obstacles within the matrix. Dislocations are responsible for plastic deformation fields around an evolving crack tip. These features require that decohesion in materials be addressed from a multi-scale standpoint. A purely atomistic approach (i.e. without mechanical defects), for example, leads to values of the peak interfacial opening stress of the order of 10GPa [1]. This is typically several orders of magnitude larger than what is observed in experiments. Plastic deformation during interfacial separation is likely to lower the atomistically-predicted peak opening stress. This requires that phenomena at both length scales be investigated and incorporated into an interfacial constitutive law that governs material separation. Such constitutive laws are current topic of research in the materials and mechanics communities.

In the present work, we focus on the effects of obstacle density and slip plane spacing on the continuum problem of dislocation nucleation, movement, pinning and annihilation in the vicinity of crack tip. The crack tip is allowed to open, but it is prevented from growing through application of a suitably high value of the peak opening stress. The peak stress and corresponding normal separation are specified by a cohesive zone law that is based upon the universal binding energy relation [2]. This law governs decohesion ahead of the crack tip. Plastic deformation is limited to a small process window that surrounds the stationary crack tip. We specifically examined some limiting case solutions for extreme obstacle densities and slip plane spacings within the small strain, discrete dislocation framework outlined in [3]: these solutions have not previously been investigated to sufficient detail. We examined materials that are representative of FCC and BCC crystals from the standpoint that they capture only two-dimensional stress states in what are otherwise three-dimensional stress states in real materials. These materials are therefore referred to as “FCC-like” and “BCC-like.” The discrete dislocation approach consists of writing the stresses and strains as a superposition of fields due to the discrete dislocations (which do not necessarily satisfy the boundary conditions) and image fields that contain the necessary degrees of freedom to satisfy the boundary conditions. An incremental finite element method using quadrilateral elements was used to solve for the image fields [4]. The elasticity solution for edge dislocations in a half-space was used [3]. Nucleation, annihilation and movement of dislocations along specified slip planes were governed by a set of constitutive rules. The active slips planes were initially dislocation free.

This work is a precursor to the next phase of the coating delamination component of the

Brown Collaborative Lab in which we shall remove the crack altogether, and apply a uniform tension to the edges of the bar. An atomistically-derived cohesive zone law will then be prescribed (instead of the heuristically-formulated cohesive zone law used in the present work) that will simulate decohesion at aluminum/diamond interfaces: this law has previously been reported in [1]. The goal of this work is to derive a new cohesive zone law that incorporates the effects of dislocation nucleation, movement/pinning, and annihilation as well as chemical bonding effects from the atomic scale, that can be used in applications where failure processes involving interfacial separation are to be modeled (e.g. coating delamination, intergranular and transgranular fracture, and debonding of hard particles). Lessons learned from this proposed work can be applied to the development of multiscale cohesive laws, including connections to crack propagation analysis in continuum and homogeneous materials.

## Method of analysis

In this analysis, a tensile bar with a pre-existing crack is subjected to simple tension as shown in Fig. 1(a). As shown in Fig. 1(b), plasticity is confined to a rectangular window surrounding the crack tip. Plastic flow is due only to the creation, motion and annihilation of discrete dislocations, and there are no dislocations beyond the boundaries of this window. The dislocations are treated as line singularities in an elastically isotropic material, with Young's modulus  $E$  and Poisson's ratio  $\nu$ . Multiple slip systems are accounted for, with slip planes being oriented symmetrically about the crack plane. Interfacial decohesion ahead of the crack tip is modeled using a cohesive zone framework where a traction-displacement separation relation describes the characteristics of the material in response to an applied traction [11]. The boundary conditions are imposed by displacements corresponding to the isotropic elastic mode I singular field remote from the crack tip ( $K_I$ -field). According to the classic theory of linear elastic fracture mechanics, the displacement components on the remote boundary are prescribed to be:

$$\begin{aligned} u_1 &= \frac{K_I}{\mu} \sqrt{\frac{r}{2\pi}} \cos \frac{\theta}{2} \left( 1 - 2\nu + \sin^2 \frac{\theta}{2} \right) \\ u_2 &= \frac{K_I}{\mu} \sqrt{\frac{r}{2\pi}} \sin \frac{\theta}{2} \left( 1 - 2\nu + \cos^2 \frac{\theta}{2} \right) \end{aligned} \quad (1)$$

where  $r = \sqrt{x_1^2 + x_2^2}$ ,  $\theta = \tan^{-1}(x_2/x_1)$  and  $\mu = E/2(1+\nu)$ , with Cartesian coordinates measured relative to the crack tip. Since boundary conditions are described in terms of the stress intensity factor  $K_I$ , the problem does not need to be described by the applied load  $\sigma_0$  and the dimensions of the bar.

## Cohesive Zone Laws

The Cohesive Zone Model (CZM) was first proposed by Dugdale [5] and Barenblatt [6] to describe material degradation and separation in a process zone in front of a crack tip in brittle materials. Since then, fracture processes in many different materials, (e.g. polymers, concrete, ceramics and composites), have been modeled with a cohesive crack. The essence of this model is the description of the non-linearity inherent in decohesion by means of a relationship between the cohesive traction and the crack opening. The constitutive description of the surrounding materials differs from that within the process zone and is introduced to avoid singular stresses around the crack as compared to linear-elastic fracture mechanics (LEFM). The model was used in the framework of finite element method by Needleman [7] to simulate the decohesion of a viscoplastic materials from a rigid substrate.

The cohesive model is introduced through cohesive “*interface*” elements in the finite element mesh. These *zero thickness* interface elements are embedded along element boundaries and are used to simulate the initiation of cracks and subsequent large sliding, opening and closing of cracked surfaces. The model assumes that a perfect interface between two surfaces carries forces that oppose separation and shear between them until decohesion. Once decohesion occurs, the two surfaces behave as distinct entities. The propagation of a crack is therefore simulated as the consecutive failure of interface elements. The cohesive relationship is expressed in terms of an effective opening displacement and an effective traction. The magnitude of the opposing forces before decohesion is a function of the relative normal and shear displacement jumps between the two surfaces.

The cohesive constitutive law used for this was obtained through differentiation of the universal binding energy relation (an approximation of the old Rydberg function) proposed by Rose et al. [2]. This is

$$T_n(\Delta_n) = -\sigma_{\max} \frac{\Delta_n}{\delta_n} \exp\left(-\frac{\Delta_n}{\delta_n} + 1\right), \quad \text{for } 0 < x_1 < x_c \quad (2)$$

where  $\Delta_n$  is the normal separation of the cohesive surface,  $T_n$  is the corresponding traction, and  $x_c$  is the length of the cohesive interface. In Eq. 2,  $\sigma_{\max}$  is the maximum cohesive strength, and  $\delta_n$  is the critical value of the normal separation in which the traction reaches its maximum value. Note that  $\sigma_{\max}$  and  $\delta_n$  are the intrinsic cohesive parameters of the material. Since only pure Mode I opening is considered in the present work, the tangential traction is neglected. As shown in Fig. 1(b), the normal to the cohesive surface is parallel to the  $x_2$ -axis so that, with the assumed

symmetry, the opening of the cohesive surface is given by  $\Delta_n = 2u_2$ . The cohesive surface is only defined from  $x_1=0$  to  $x_c$ . For  $x_1 \geq x_c$ , symmetry conditions are prescribed, such that  $u_2 = 0$  and  $T_1 = 0$ . Note that the area under the  $T_n$  vs.  $\Delta_n$  curve is the ideal work of adhesion (or work of separation) and is given by the following expression:

$$\phi_n = \int_0^\infty T_n(\Delta_n) d\Delta_n = e\sigma_{\max}\delta_n \quad (3)$$

### Discrete Dislocation Theory

Within the process window of Fig. 1(b), dislocations are treated as line singularities immersed in an elastically isotropic material. The quasi-static deformation process leads to the generation, motion and annihilation of these dislocations as governed by a set of constitutive rules. Assuming dislocation glide only, the variation of the potential energy of the body due to infinitesimal variations of the  $I$ th dislocation is governed by the Peach-Koehler force:

$$f^{(I)} = n_i^{(I)} \left( \hat{\sigma}_{ij} + \sum_{J \neq I} \sigma_{ij}^{(J)} \right) b_j^{(I)} \quad (4)$$

with  $n_i^{(I)}$  the slip plane normal and the Burgers vector  $b_i^{(I)}$  of dislocation  $I$ . The direction of this force is in the slip plane and normal to the dislocation line. The Peach-Koehler force includes the long-range interactions with all other dislocations in the material. It is this force that will determine the evolution of the dislocation structure, accounting for glide, generation, annihilation and pinning at obstacles according to a set of rules to be discussed shortly.

The magnitude of the glide velocity  $v^{(I)}$  of dislocation  $I$  is taken to be linearly related to the Peach-Koehler force through the drag relation,

$$f^{(I)} = Bv^{(I)} \quad (5)$$

where  $B$  is the drag coefficient. Near dislocation pile-ups the position of dislocations is unstable leading to high velocity oscillatory motions. In order to avoid these irrelevant vibrations, a cut-off velocity is applied. For the material parameters used in this work, Cleveringa et al. [3] have found that a cut-off velocity of 20 m/s is low enough to allow substantially increased time steps and high enough so as not to significantly affect the results. New dislocation pairs are generated by simulating Frank-Read sources. The initial dislocation segment of a Frank-Read source bows out until it produces a new dislocation loop and a replica of itself (See Figure 2(a)). The Frank-Read

source is modeled in terms of a critical value of the Peach-Koehler force, the time it takes to generate a dislocation loop and the size of the generated loop. As shown in Figure 2(b) for two dimensions, this is simulated by point sources that generate a dislocation dipole when the magnitude of the Peach-Koehler force at the source exceeds a critical value  $\tau_{nuc} b$  during a period of time  $t_{nuc}$ . The distance  $L_{nuc}$  between the dislocations is given by

$$L_{nuc} = \frac{E}{4\pi(1-\nu^2)} \frac{b}{\tau_{nuc}} \quad (6)$$

At this distance, the shear stress of one dislocation acting on the other is balanced by the slip plane shear stress  $\tau_{nuc}$ . Two dislocations with opposite Burgers vector will annihilate when they are sufficiently close together. This is modeled by eliminating two dislocations when they are within a material-dependent, critical annihilation distance  $L_e$ . Obstacles to dislocation motion are modeled as fixed points on a slip plane. Such obstacles account for the effects of small precipitates or dislocations on other slip systems in blocking slip. Pinned dislocations can only pass the obstacles when their Peach-Koehler force exceeds an obstacle dependent value,  $\tau_{obs} b$ .

It is noted that the above rules for dislocation evolution are intended to incorporate short-range effects at an atomic scale, which a discrete dislocation model could not otherwise resolve. Short-range interactions between dislocations on different slip planes, even near slip plane junctions, are not accounted for separately in this analysis; such dislocations only interact through their long-range elastic fields.

When a dislocation glides into the open crack it can disappear from the material. We model this by taking the dislocation out of the system. The number of dislocations that leave each slip plane is stored. Since the analytical formulas used for the stress and displacement describe the dislocation in a half-space with a traction-free surface, a dislocation located at the surface makes no contribution to the stress field. However, there is a contribution to the displacement field, with a step of  $b/2$  across the slip plane at the surface.

Because of the assumed symmetry, there is a mirror dislocation for each dislocation in the region analyzed numerically. This mirror dislocation does not need to be accounted for explicitly when superimposing the fields of all dislocations, for example as in the Peach-Koehler force  $f^{(I)}$ . Rather, its presence is accounted for through the symmetry boundary conditions. What does need to be accounted for in the dislocation analysis is that when a dislocation crosses the closed crack plane, it leaves the plasticity region, but, due to symmetry, a mirror dislocation enters into the system along the mirror slip plane.

## Incremental analysis

The stress and deformation fields are obtained in an incremental manner as described in detail by Cleveringa et al. [3]. In each time increment, the energy stored in the material must be balanced by the energy due to the applied and cohesive tractions. The dislocation distribution is updated according to the above rules for dislocation motion, generation, annihilation and pinning, and the increment in the fields is solved from the incremental version of the virtual work equation:

$$\int_V \{\delta\boldsymbol{\varepsilon}\}^T \{\boldsymbol{\sigma}\} dV - \frac{1}{2} \int_{S_{coh}} \{\delta\boldsymbol{\Delta}\}^T \{\boldsymbol{T}\} dS = \int_{S_{ext}} \{\delta\boldsymbol{u}\}^T \{\boldsymbol{T}\} dS \quad (7)$$

where  $V$  is the volume of the region analyzed,  $S_{ext}$  is the external surface and  $S_{coh}$  is the surface across which cohesive tractions operate.  $\{\boldsymbol{u}\}^T = (u_1, u_2)$  is the displacement field vector and  $\{\boldsymbol{\Delta}\}^T = (\Delta_n, \Delta_t)$  is the displacement jump vector across the cohesive surface. The stress and strain vectors are given by  $\{\boldsymbol{\sigma}\}^T = (\sigma_{11}, \sigma_{22}, \sigma_{12})$  and  $\{\boldsymbol{\varepsilon}\}^T = (\varepsilon_{11}, \varepsilon_{22}, \varepsilon_{12})$ , respectively. The  $\sigma_{ij}$  are the components of the stress tensor, and the strain is defined as  $\varepsilon_{ij} = \frac{1}{2}(u_{i,j} + u_{j,i})$ . The factor of  $\frac{1}{2}$  in Eq. (7) is given by the symmetry of the problem: only one half of the work in the cohesive surface contributes to the work in the region analyzed.

As discussed in Cleveringa et al. [3], the velocity, strain-rate and stress-rate fields are written as the superposition of two fields,

$$\dot{u}_i = \tilde{u}_i + \hat{u}_i, \quad \dot{\varepsilon}_{ij} = \tilde{\varepsilon}_{ij} + \hat{\varepsilon}_{ij}, \quad \dot{\sigma}_{ij} = \tilde{\sigma}_{ij} + \hat{\sigma}_{ij} \quad (8)$$

The ( $\tilde{\quad}$ ) fields are the fields due to the individual dislocations in their current configuration; this gives rise to tractions  $\tilde{T}_i$  and displacements  $\tilde{U}_i$  on the boundary of the body. The ( $\hat{\quad}$ ) fields represent the image fields that correct for the actual boundary conditions. Figure 3 shows this decomposition for the problem to be solved in this work.

At a given time  $t$ , the stress field and the current positions of all dislocations are known. An increment of loading  $\dot{K}_I \Delta t$  is prescribed. The rate boundary value problem is formulated by expanding the virtual work balance at  $t + \Delta t$ . Eq. (7) is written as:

$$\int_V \{\delta\boldsymbol{\varepsilon}\}^T \{\hat{\boldsymbol{\sigma}}^{t+\Delta t}\} dV - \frac{1}{2} \int_{S_{coh}} \{\delta\boldsymbol{\Delta}\}^T \{\boldsymbol{T}^{t+\Delta t}\} dS = 0 \quad (9)$$

assuming zero traction on the external surface  $S_{ext}$  where the tractions are prescribed, and by invoking  $\{\delta u\}=0$  on the part of the external surface where the displacements are prescribed. Also the normal part of the cohesive traction law is considered  $\{\Delta\}=(\Delta_n,0)$ . We require that the dislocation field  $\{\tilde{\sigma}\}$  satisfy continuing equilibrium together with traction-free conditions on  $x_2=0$ , so that  $\int_V \{\delta \varepsilon\}^T \{\tilde{\sigma}\} dV = 0$ .

As given in Cleveringa et al. [3], the cohesive traction is expanded in a Taylor series about the time  $t + \Delta t$

$$T_n(\Delta_n^{t+\Delta t}) = T_n(\tilde{\Delta}_n^{t+\Delta t} + \hat{\Delta}_n^t) - K_{coh}(\tilde{\Delta}_n^{t+\Delta t} + \hat{\Delta}_n^t) \hat{\Delta}_n^t \Delta t \quad (10)$$

where  $\tilde{\Delta}_n$  and  $\hat{\Delta}_n$  are related to the corresponding displacement fields,  $\tilde{u}_2$  and  $\hat{u}_2$ , and  $K_{coh} = -\frac{\partial T_n}{\partial \Delta_n}$ . Using Eq. (10) and the first order approximation for the stress-rate  $\hat{\sigma}_{ij}^{t+\Delta t} = \hat{\sigma}_{ij}^t + \hat{\sigma}_{ji} \Delta t$ , the principle of virtual work Eq. (9) becomes

$$\int_V \{\delta \varepsilon\}^T \{\hat{\sigma}\} dV + \frac{1}{2} \int_{S_{coh}} \{\delta \Delta_n\}^T K_{coh} \{\hat{\Delta}_n\} dS = -\frac{1}{\Delta t} \left[ \int_V \{\delta \varepsilon\}^T \{\hat{\sigma}^t\} dV - \frac{1}{2} \int_{S_{coh}} \{\delta \Delta_n\}^T \{T_n\} dS \right] \quad (11)$$

where  $K_{coh}$  and  $T_n$  are evaluated for  $\Delta_n^* = \tilde{\Delta}_n^{t+\Delta t} + \hat{\Delta}_n^t$ . The equation contains two terms for the bulk and cohesive behavior and the right-hand side, which is known at time  $t + \Delta t$ .

## Finite element formulation

Eq. (11) gives the weak form to be used in the finite element formulation that is presented in this section. In order to derive the final linear system to be solved at time  $t + \Delta t$ , we assume that we know the strain-displacement matrix  $[B]$  that relates the strain to the nodal displacement vector and the matrix  $[N_{coh}]$  that relates the cohesive displacement jumps to the nodal displacements. Considering the *hat*-stress-rate  $\{\hat{\sigma}\} = [E] \{\hat{\varepsilon}\}$  and the *hat*-strain rate  $\{\hat{\varepsilon}\} = [B] \{\hat{d}\}$ , the first term of Eq. (11) can be written as

$$\int_V \{\delta \varepsilon\}^T \{\hat{\sigma}\} dV = \{\delta d\}^T \int_V [B]^T [E] [B] dV \{\hat{d}\} \quad (12)$$

where  $\{\delta\mathcal{E}\}^T = \{\delta d\}^T [B]^T$ . Using  $\{\hat{\Delta}_n\} = 2[N_{coh}] \{\hat{d}\}$ ,  $\{\delta\Delta_n\}^T = 2\{\delta d\}^T [N_{coh}]^T$ , the second term becomes

$$\frac{1}{2} \int_{S_{coh}} \{\delta\Delta_n\}^T K_{coh} \{\hat{\Delta}_n\} dS = \{\delta d\}^T \frac{1}{2} \int_{S_{coh}} 2[N_{coh}]^T K_{coh} 2[N_{coh}] dS \{\hat{d}\} \quad (13)$$

Using the same idea, the terms of the right hand side can be written as

$$\int_V \{\delta\mathcal{E}\}^T \{\hat{\sigma}^t\} dV = \{\delta d\}^T \int_V [B]^T \{\hat{\sigma}^t\} dV \quad (14)$$

and

$$\frac{1}{2} \int_{S_{coh}} \{\delta\Delta_n\}^T \{T_n\} dS = \{\delta d\}^T \frac{1}{2} \int_{S_{coh}} 2[N_{coh}]^T \{T_n\} dS \quad (15)$$

Finally Eqs. (12) - (15) are replaced in the weak form of Eq. (11) as follows

$$\{\delta d\}^T \left( \left[ \int_V [B]^T [E][B] dV + \int_{S_{coh}} 2[N_{coh}]^T K_{coh} [N_{coh}] dS \right] \{\hat{d}\} + \frac{1}{\Delta t} \left[ \int_V [B]^T \{\hat{\sigma}^t\} dV - \int_{S_{coh}} [N_{coh}]^T \{T_n\} dS \right] \right) = 0$$

(16)

Since Eq. (16) has to be valid for any  $\{\delta d\} \neq 0$ , it implies the following linear system:

$$([K] + [K_{coh}]) \{\hat{D}\} = \{R\} \quad (17)$$

where

$$[K] = \int_V [B]^T [E][B] dV \quad (18)$$

and

$$[K_{coh}] = \int_{S_{coh}} 2[N_{coh}]^T K_{coh} [N_{coh}] dS \quad (19)$$

are the bulk stiffness matrix and cohesive stiffness matrix, respectively. The right hand side of Eq.

(17) is given by

$$\{R\} = \frac{1}{\Delta t} \left[ \int_V [B]^T \{\hat{\sigma}^t\} dV - \int_{S_{coh}} [N_{coh}]^T \{T_n\} dS \right] \quad (20)$$

In Eq. (17),  $\{\hat{D}\}$  is the global nodal *hat*-displacement rate vector.

## Limiting Cases

### FCC-like orientation

The region analyzed in this report is  $1000 \times 500 \mu\text{m}^2$ . Inside the process window of  $45 \times 45 \mu\text{m}^2$  the mesh is refined with elements of size  $h=0.5 \mu\text{m}$ . In all cases, the crystal has three slip systems at  $\pm 54.75^\circ$  and  $0^\circ$  with respect to the crack plane  $x_2 = 0$ . For each slip system there are 1500 slip planes equally spaced over the process window, with a spacing of  $d_s=120b$ . Initially, these slip planes are assumed not to have any mobile dislocations, but to have a random distribution of dislocation sources and obstacles. The value of the drag coefficient is taken as  $B = 10^{-4} \text{ Pa s}$ , which is a representative value for aluminum (Kubin et al., 1992). The strength of the dislocation sources is randomly chosen from a Gaussian distribution with mean strength  $\bar{\tau}_{nuc} = 50 \text{ MPa}$  and standard deviation  $0.2\bar{\tau}_{nuc}$ . The mean nucleation distance is  $L_{nuc} = 125b$  and  $b$  is specified to have the value  $0.25 \text{ nm}$ . The nucleation time for all sources is taken as  $t_{nuc} = 10 \text{ ns}$ . All obstacles are taken to have the same strength,  $\tau_{obs} = 150 \text{ MPa}$ . The annihilation distance is specified as  $L_e = 6b$ . The elastic constants for aluminum are  $E = 70 \text{ GPa}$  and  $\nu = 0.33$ .

The cohesive surface properties are taken to be  $\sigma_{max} = 3 \text{ GPa}$  and  $\delta_n = 50 \text{ nm}$  ( $= 200b$ ) giving a work of separation,  $\phi_n = 407.7 \text{ J/m}^2$ . The cohesive parameters  $\sigma_{max}$  and  $\delta_n$  (and therefore  $K_0$ ) have been chosen such that crack propagation is inhibited during the calculation, though crack opening can occur. For fracture without any dislocation activity where all energy released is consumed by the cohesive surface, unstable crack growth occurs at an applied stress intensity factor  $K_0$  (Rice, 1968):

$$K_0 = \sqrt{\frac{E\phi_n}{1-\nu^2}} \quad (21)$$

For the chosen material parameters,  $K_0 = 5.66 \text{ MPa m}^{1/2}$ . All calculations have been carried out for an applied loading rate specified by  $\dot{K}_I = 100 \text{ GPa m}^{1/2}/\text{s}$ .

### 1) Effect of obstacle density:

In order to study the dependence of the density of obstacles on the deformation of the material in the vicinity of the crack, five obstacle densities were considered,  $\rho_{obs} = 0, 8.4, 25.4, 51.7$  and  $103.4 \mu m^{-2}$  in addition to the elastic limit. Initially, there are no mobile dislocations and the density of nucleation sites (or sources) is the same for all cases,  $\rho_{nuc} = 51.7 \mu m^{-2}$ . The time increment is specified to be  $\Delta t_{incr} = 0.5 ns$  with load steps of  $\Delta K_I/K_0 = 8.8 \times 10^{-6}$ . The calculations were carried out for  $4.5 \mu sec$  (9000 increments) until  $K_I/K_0 = 0.08$ . Although  $K_I/K_0$  is low compared with previous numerical simulations reported in the literature (see for example Cleveringa et al. [3] and Deshpande et al., [9]), the final stress intensity factor  $K_I = 0.45 MPa m^{1/2}$  is high enough to develop plastic deformation. A problem arose at the lowest obstacle density in that dislocations piled up near the edges of the process windows for relatively low values of  $K_I$ : this invalidated the results. In order to circumvent this problem a larger process window was considered ( $45 \times 45 \mu m^2$ ) for our analysis of different obstacle densities.

Figure 4 shows the normalized opening stress  $\sigma_{22}/\tau_{nuc}$  for the five obstacle densities at  $K_I/K_0 = 0.08$  in the process window. In addition, the mode I elastic crack tip field (Fig. 4(f)) has been included for comparison purposes. The plots only show the stresses extrapolated to the nodes of the mesh. Therefore, the locally high stresses near the dislocations cannot be displayed. Since crack propagation is inhibited, more dislocation activity occurs, even for the case with the highest density of obstacles. Two limiting cases were considered in these figures: the case with  $\rho_{obs} = 0$  and the case with  $\rho_{obs} = 103.4 \mu m^{-2}$  (Figs. 4a,e respectively). For the case with no obstacles, the dislocations can move freely through the process window and, therefore, leading to plastic deformation. For the case with more obstacles, however, the density of dislocations in a small area about the crack tip is larger than the case with no obstacles. This means that dislocations created by the stress concentration get pinned at the obstacles near the crack tip. The results for the intermediate obstacle densities are shown in Figs. 4(b) 4(c), and 4(d). The net effect of increasing the obstacle density is therefore to decrease the ductility of the material. Figure 4(f) is the limiting case where no plastic deformation is allowed in the process window.

A closer look at the dislocation structure near the crack tip shows another interesting trend. Figure 5 shows magnified views of the process windows near the crack tip for the two limiting cases,  $\rho_{obs} = 0, 103.4 \mu m^{-2}$ . These figures emphasize the substantial differences in the variation of  $\sigma_{22}/\tau_{nuc}$  between these obstacle densities. In Fig. 5(a), we note that the highest opening stresses are in the immediate vicinity of the crack tip since dislocations freely propagate away from the crack tip in the absence of obstacles. However, in Fig. 5(b), the highest open stresses are found in a larger area behind of the crack tip since dislocation motion is impeded by the high obstacle density. Note that the creation and annihilation of dislocations in the process window is not very

sensitive to the obstacle density.

Figures 6 and 7 show the distribution of total slip (which is a measure of plastic deformation), defined as

$$\Gamma = \sum_{\alpha=1}^3 |\gamma^{(\alpha)}| \quad (22)$$

where

$$\gamma^{(\alpha)} = s_i^{(\alpha)} \varepsilon_{ij} m_j^{(\alpha)} \quad (23)$$

and  $s_i^{(\alpha)}$  and  $m_j^{(\alpha)}$  are the tangent and normal to the slip plane  $\alpha$ , respectively, at selected obstacle densities. The plastic deformation patterns in terms of distribution of slip are calculated from the computed displacement field at  $K_I/K_0 = 0.8$ . Although the displacement field is not continuous due to the existence of displacement jumps across slip planes, for visualization purposes, the strain is computed as  $\varepsilon_{ij} = (u_{i,j} + u_{j,i}) / 2$ .

Figure 6 shows the total slip computed from the sum elastic and plastic strains. Contours tend to be “rounded” for the cases with more obstacles indicating a tendency for a more elastic deformation field. In contrast, the case with no obstacles presents localized shear bands along the more active slip planes. This localization is more evident for the contours of the total “plastic” slip shown in Figure 7, where the plastic deformation disappears as the obstacle density increases and becomes more significant as the obstacle density decreases. In order to compute the total “plastic” slip, the strains were computed using only the contribution from the dislocation activity. This demonstrates one more time that the effect of including more obstacles into the system makes the material less ductile. On the other hand, when dislocations are allowed to move freely into the process window, the plastic deformation is more spread out thereby shielding the crack tip. Energy is absorbed by plastic deformation and this tends to prohibit crack growth and enhances crack blunting. Figure 8(a) plots the geometry of the crack shape at different obstacle densities. Close examination of the crack shape shows that the crack blunts for the limiting case of no obstacles, but tends to the elastic solution (brittle fracture) at high obstacle densities. Finally, the size of this developing plastic zone can be quantified by measuring the radius of the smallest circle centered at the crack tip containing only the plastic deformation. Figure 8(b) shows the plastic zone size vs. the obstacle density at  $K_I/K_0 = 0.8$ . The plastic zone can vary from  $r_p=42.5 \mu m$  for 0 dislocations down to  $r_p=13.3 \mu m$  for the maximum density considered in this work ( $\rho_{obs} = 103.4 \mu m^{-2}$ ), which represents a reduction of 70%.

## 2) Effect of slip plane spacing:

The effect of the spacing between slip planes,  $d_s$ , is considered in this section. Four cases are analyzed in which only the number of planes through the process window was varied. The following values for slip plane spacing were considered: (a)  $d_s = 240b$  ( $\rho_{nuc} = \rho_{obs} = 26 \mu m^2$ ), (b)  $d_s = 120b$  ( $\rho_{nuc} = \rho_{obs} = 52.3 \mu m^2$ ) (c)  $d_s = 80b$  ( $\rho_{nuc} = \rho_{obs} = 78.4 \mu m^2$ ), and (d)  $d_s = 60b$  ( $\rho_{nuc} = \rho_{obs} = 104.53 \mu m^2$ ). For each case, the number of obstacles and sources per slip plane were equivalent; however, the total density is different from case-to-case due to the spacing differences. Since none of these cases had zero obstacles the process window area was reduced to  $30 \times 30 \mu m^2$ .

Figure 9 shows the normalized opening stress  $\sigma_{22}/\tau_{nuc}$  for these four cases at  $K_I/K_0 = 0.08$ . The case shown Fig. 9(b) for  $d_s = 120b$ , is equivalent to the problem described in the previous section (for  $\rho_{obs} \approx 50 \mu m^2$ ). This figure gives the impression that plastic deformation increases for shorter slip plane spacings. The cases with fewer slip planes (longer  $d_s$ ) show a smaller amount of dislocations than the cases with more planes (see Fig. 9a).

Figures 10 and 11 show the total slip and the “plastic” total slip, respectively, for the two extreme slip plane spacings of  $d_s = 240b$  and  $60b$ . Plastic deformation is more evident in the cases with a higher density of planes. It is important to keep in mind that, even though the obstacle density increases with the number of planes, the source density increases at an equal rate. Hence, the effect of increasing the obstacle density is counteracted by a concurrent increase in the sources. Figure 11 shows a decrease of 60%, from \_\_\_\_\_ to \_\_\_\_\_, in the plastic zone size when the spacing between active slip planes is increased from  $d_s = 60b$  to  $240b$ .

Figure 12 shows the evolution of the dislocation density with  $K_I/K_0$  for the different cases. In order to compute the dislocation density, the total number of dislocations is divided by the area of the process window. Unlike the case studied in the previous section, the total dislocation density changes for each case. The shorter the distance between planes the greater the number of nucleation sites, thus the greater probability that dislocations will nucleate. However, Fig. 13 shows that when comparing results from varied slip plane spacing, the crack shape does not significantly depend upon the dislocation density.

### **BCC-like orientation**

A process window of  $30 \times 30 \mu m^2$  was found to be sufficient to prevent dislocations from reaching the boundary for the BCC-like orientation. In the cases analyzed in this section, the crystal has three slip systems at  $\pm 35.25^\circ$  and  $90^\circ$  with respect to the crack plane along  $x_2 = 0$ . As in previous cases, there are initially no dislocations and the density of nucleation sites (or sources) is the same for all the cases, i.e.,  $\rho_{nuc} = 66 \mu m^2$ . For each slip system the slip plane spacing is  $d_s = 120b$ . In order to make a comparison with the limiting cases presented for the fcc-like orientation, only two obstacles densities were considered,  $\rho_{obs} = 16 \mu m^2$  and  $\rho_{obs} = 66 \mu m^2$  (the

latter can be compared with the FCC case in which  $\rho_{obs} \approx 50 \mu m^{-2}$ ).

Figure 14 shows the normalized opening stress  $\sigma_{22}/\tau_{nuc}$  for the two obstacle densities at  $K/K_0 = 0.08$ . It is evident from these plots that dislocation activity is stronger on the slip planes perpendicular to the crack plane. Figure 15 and 16 show the total slip and “plastic” slip, respectively, where substantial localized plastic deformation is observed along the  $90^\circ$  planes.

Figure 17 shows the crack shape at selected obstacle densities. As was the case with the fcc-like material, the crack shape does not show a strong dependence upon the obstacle density. The evolution of the dislocation density for these two BCC-like cases are plotted together with the previous FCC-cases in Figure 18. It is observed that the density is significantly lower than the fcc-like orientation due to differences in slip plane orientation.

## Summary

Within the context of small strain, discrete dislocation theory, we examined the effects of obstacle and slip plane density on the stress field in the vicinity of a crack tip. The nonlinearities associated with interfacial decohesion ahead of the crack tip was governed by a cohesive zone law that specifies the peak opening traction and corresponding interfacial opening distance. Dislocation nucleation, movement, annihilation and pinning were modeled with a set of constitutive rules. We examined FCC-like and BCC-like materials that differed in slip plane orientation only. The most significant conclusions from this work are as follows:

(1) The ductility of both FCC-like and BCC-like materials is decreased as the density of obstacles within the material is increased. Dislocation motion is effectively decreased as dislocations become pinned at obstacles within the process window that surrounds the crack tip. The plastic zone size for the case without obstacles is  $r_p = 42.5 \mu m$ . However, it is shown that the plastic zone size is reduced by 70% when an obstacle density of  $\rho_{obs} = 103.4 \mu m^{-2}$  is considered.

(2) Crack tip shielding occurs at small obstacle densities in both materials since dislocations are free to move in the process window, and this promotes crack blunting rather than crack growth.

(3) For both materials, dislocation movement and hence plastic deformation increases when active slip planes are more closely spaced. A decrease of 60% in the plastic zone size is noticed when the spacing between active slip planes is increased from  $d_s = 60b$  to  $240b$ .

(4) For the BCC-like material, dislocation activity is strongest along the  $90^\circ$  plane. For the FCC-like

material, dislocation activity is strongest along the  $\pm 54.75^\circ$  planes.

(5) For the same obstacle and slip plane densities, the dislocation density (at each loading stage) in BCC-like materials is significantly lower than in FCC-like materials, this is due to slip plane orientation. For instance, at  $K_I/K_0 = 0.07$ , the dislocation density for the BCC case is only 70% of the dislocation density for the FCC case. The same has been previously observed in the behavior of a propagating crack [14].

The next step in this work is to incorporate an atomistically-derived cohesive zone law into the present formulation with the crack removed altogether. The block will then be subject to an applied tension and crack nucleation will result as an outcome of the deformation process, location of dislocations and obstacles, etc. instead of the presumption of a pre-existing crack. A new cohesive zone law will then be generated which contains effects from both chemical bonding at the atomistic scale and small strain plasticity due to dislocation motion within the entire block.

## **Acknowledgments**

The authors wish to acknowledge Nancy Johnson and Y.T. Cheng for their enthusiastic support of this work. Special thanks are due to Dr. Vikram Dehpande from Cambridge University for his helpful comments and kind assistance on the understanding of the model and code.

## REFERENCES

1. Qi, Y and Hector, Jr., L.G., "First Principles Study of Adhesion and Adhesive Transfer at Aluminum/Diamond Interfaces. Part 1. Al(111)/C(111)-1x1 and Al(111)/C(111)-(1x1):H," GM R&D Report 9424.
2. Rose, J.H., Ferrante, J., Smith, J., "Universal binding energy curves for metal and bimetallic interfaces", Phys. Rev. Lett. 47, pp. 675-678, 1981.
3. Cleveringa, H.H.M., Van der Giessen, E. and Needleman, A., "A discrete dislocation analysis of mode I crack growth", J. Mech. Phys. Solids, 48, p. 1133-1157, 2000.
4. The Brown University discrete dislocation code was used in this work.
5. Dugdale, D.S., "Yielding of steel sheets containing slits", J. Mech. Phys. Solids, 8, pp. 100-8, 1960.
6. Barenblatt G.I., "The mathematical theory of equilibrium cracks in brittle fracture", Adv. Appl. Mech., 7, pp. 55-129, 1962.
7. Needleman, A.. "An analysis of tensile decohesion along an interface". J. Mech. and Phys. Solids, 38, pp. 289-324, 1990.
8. Zavattieri P.D., "Numerical aspects of the dynamic crack growth simulation in 2-D using cohesive interfaces", GM Research report, VAD 57, 2001.
9. Deshpande V.S., Needleman, A. and Van der Giessen, E., "A discrete dislocation analysis of near-threshold fatigue crack growth", Acta Mater. 49, p. 3189-3203, 2001.
10. Kubin, L.P., Canova, G. Condat, M., Devincere, B., Pontikis, V., Bréchet, Y., "Dislocation microstructures and plastic flow: a 3D simulation", Solid State Phenomena, 23/24, p. 255-472, 1992.
11. Needleman, A., " A continuum model for void nucleation by inclusion debonding", Journal of App. Mech. 54, pp. 525-531, 1987.
12. Rice, J.R, "A path independent integral and the approximate analysis of strain concentration by notches, cracks", J. of App. Mech. 35, p. 379-386, 1968
13. Van der Giessen E. and A. Needleman, A., "Discrete dislocation plasticity: a simple planar model", Modelling Simul. Mater. Sci. Eng. 3, p. 689-735, 1995
14. Jean Gullickson, "Directional dependence of crack growth in crystals", M.Sc. Thesis, Brown University, 2003.



## FIGURES

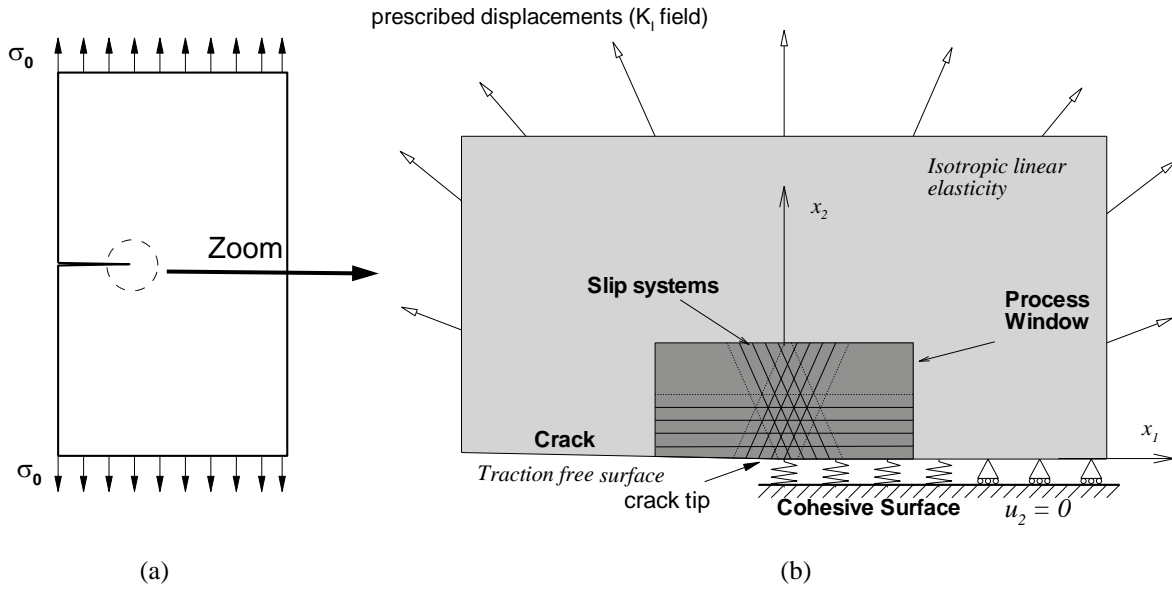


**Figure 1:** Mode I crack analysis with the discrete dislocation model and cohesive interfaces. Because of symmetry, only half the problem needs to be analyzed.

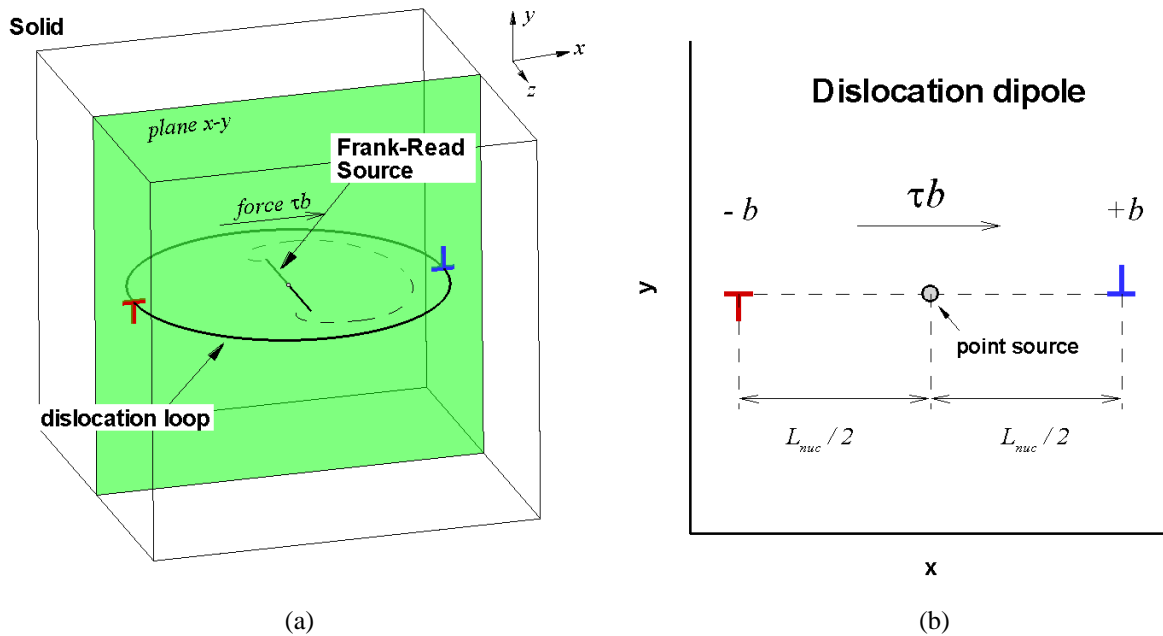


**Figure 2:** In two dimensions the dislocation loop is projected into the plane and modeled by a dislocation dipole. The Frank-Read source is modeled by a point source given by the projection of the real source into the plane  $x$ - $y$ .

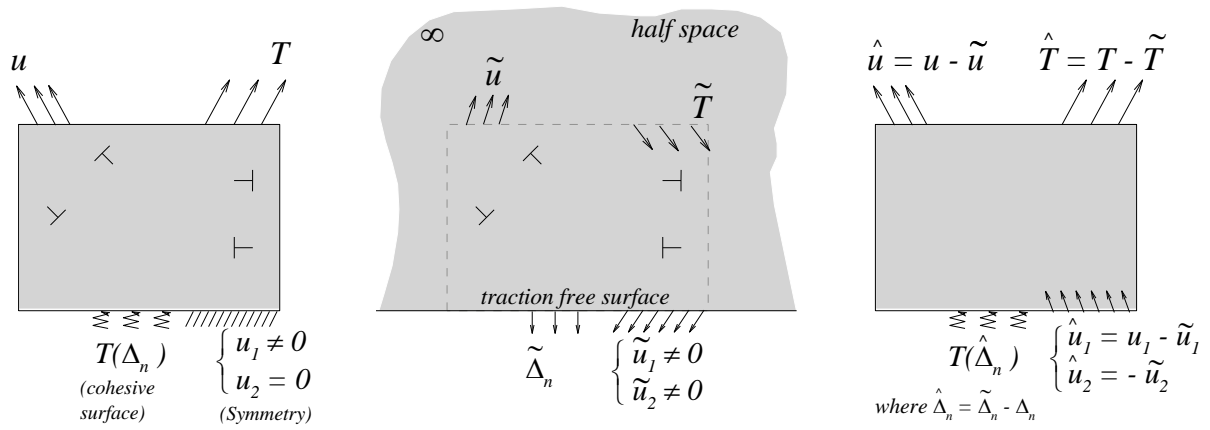


**Figure 3:** Decomposition of the problem into the problem of interacting dislocation in the homogeneous free-traction half space ( $\tilde{\cdot}$  fields) and the complementary problem of the elastic body without dislocations ( $\hat{\cdot}$  fields).

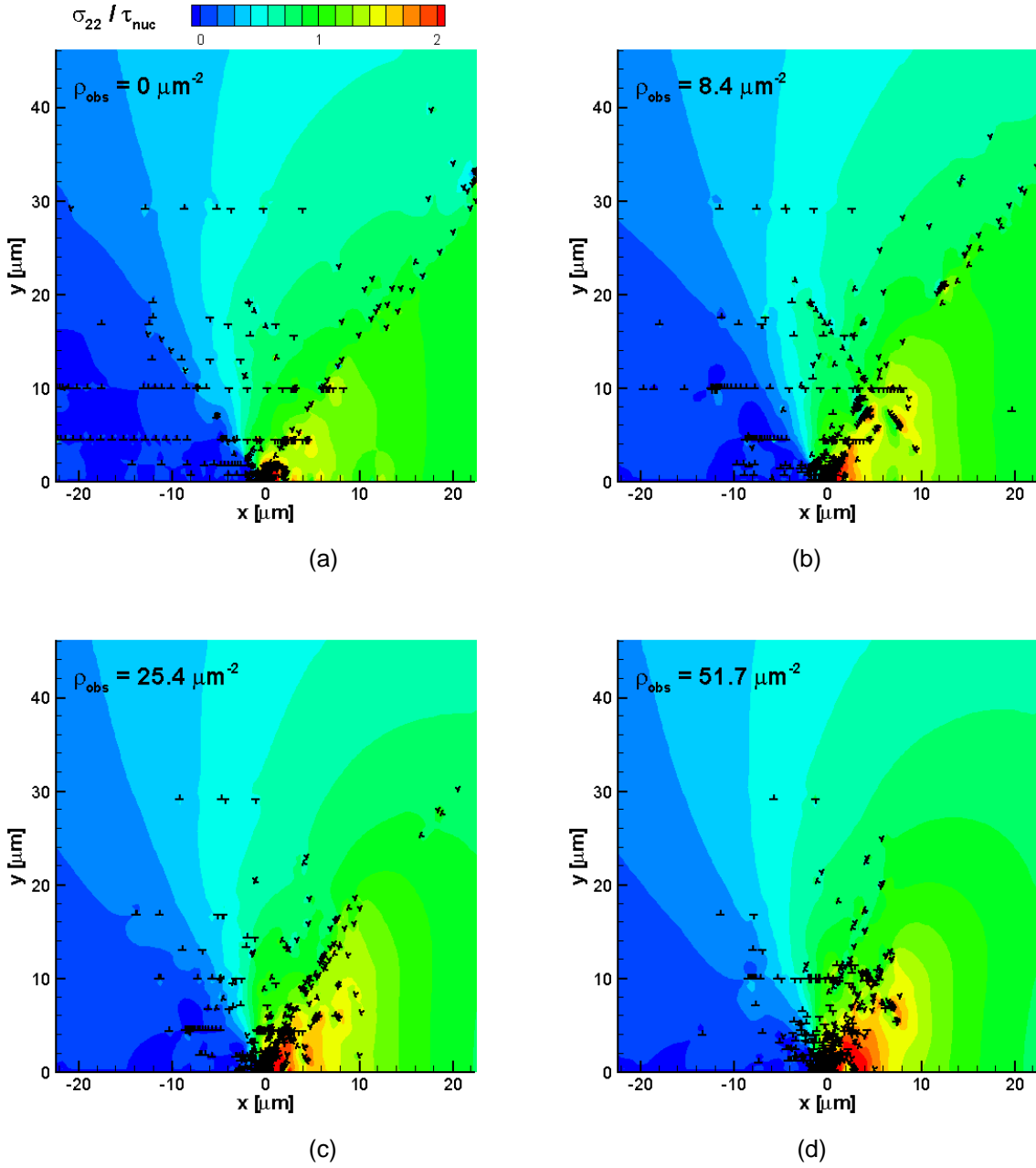


**Figure 4:** Normalized opening stress  $\sigma_{22}/\tau_{nuc}$  and dislocation distribution at  $K_I/K_0 = 0.08$ . (a)  $\rho_{obs} = 0 \mu\text{m}^{-2}$ , (b)  $\rho_{obs} = 8.4 \mu\text{m}^{-2}$  (c)  $\rho_{obs} = 25.4 \mu\text{m}^{-2}$  (d)  $\rho_{obs} = 51.7 \mu\text{m}^{-2}$  (e)  $\rho_{obs} = 103.4 \mu\text{m}^{-2}$  (f) Elastic solution.

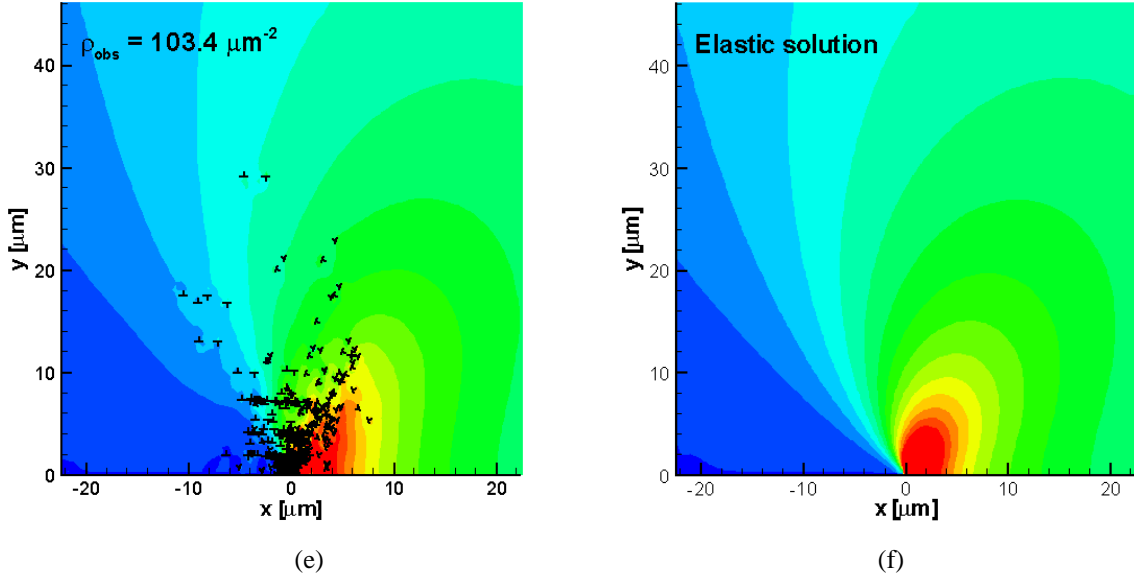


**Figure 4 (cont.):** Normalized opening stress  $\sigma_{22}/\tau_{nuc}$  and dislocation distribution at  $K_I/K_0 = 0.08$ . (a)  $\rho_{obs} = 0 \mu\text{m}^{-2}$ , (b)  $\rho_{obs} = 8.4 \mu\text{m}^{-2}$  (c)  $\rho_{obs} = 25.4 \mu\text{m}^{-2}$  (d)  $\rho_{obs} = 51.7 \mu\text{m}^{-2}$  (e)  $\rho_{obs} = 103.4 \mu\text{m}^{-2}$  (f) Elastic solution.

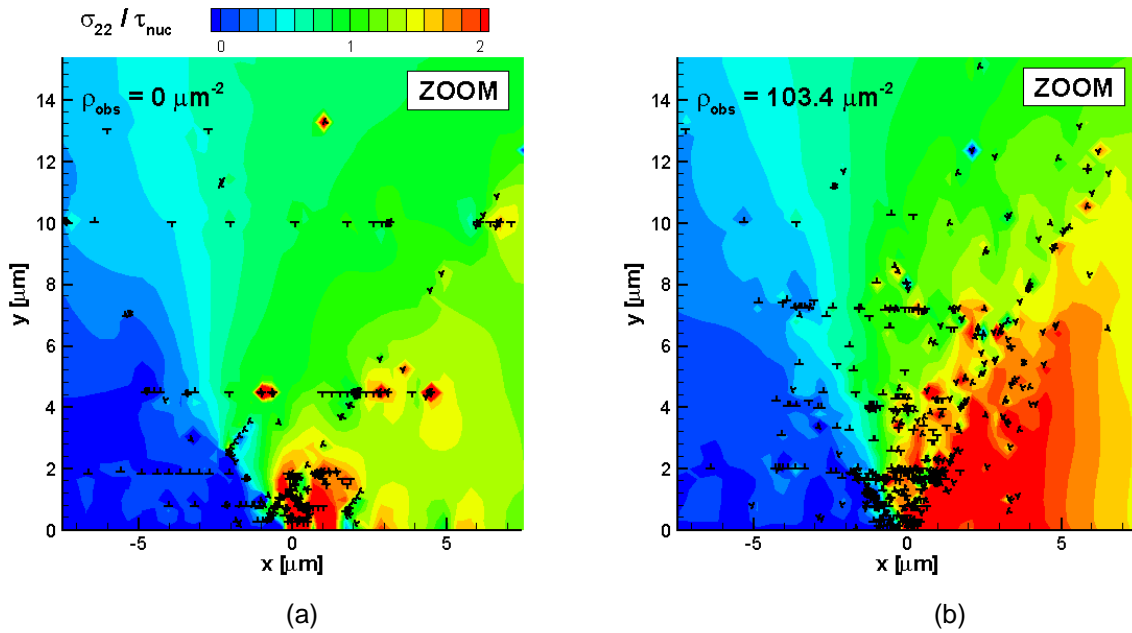


**Figure 5:** Zoom ( $15 \times 15 \mu\text{m}$ ) showing the normalized stress and dislocation distribution at  $K_I/K_0 = 0.08$  for the two limiting cases: (a)  $\rho_{obs} = 0 \mu\text{m}^{-2}$ , (b)  $\rho_{obs} = 103.4 \mu\text{m}^{-2}$

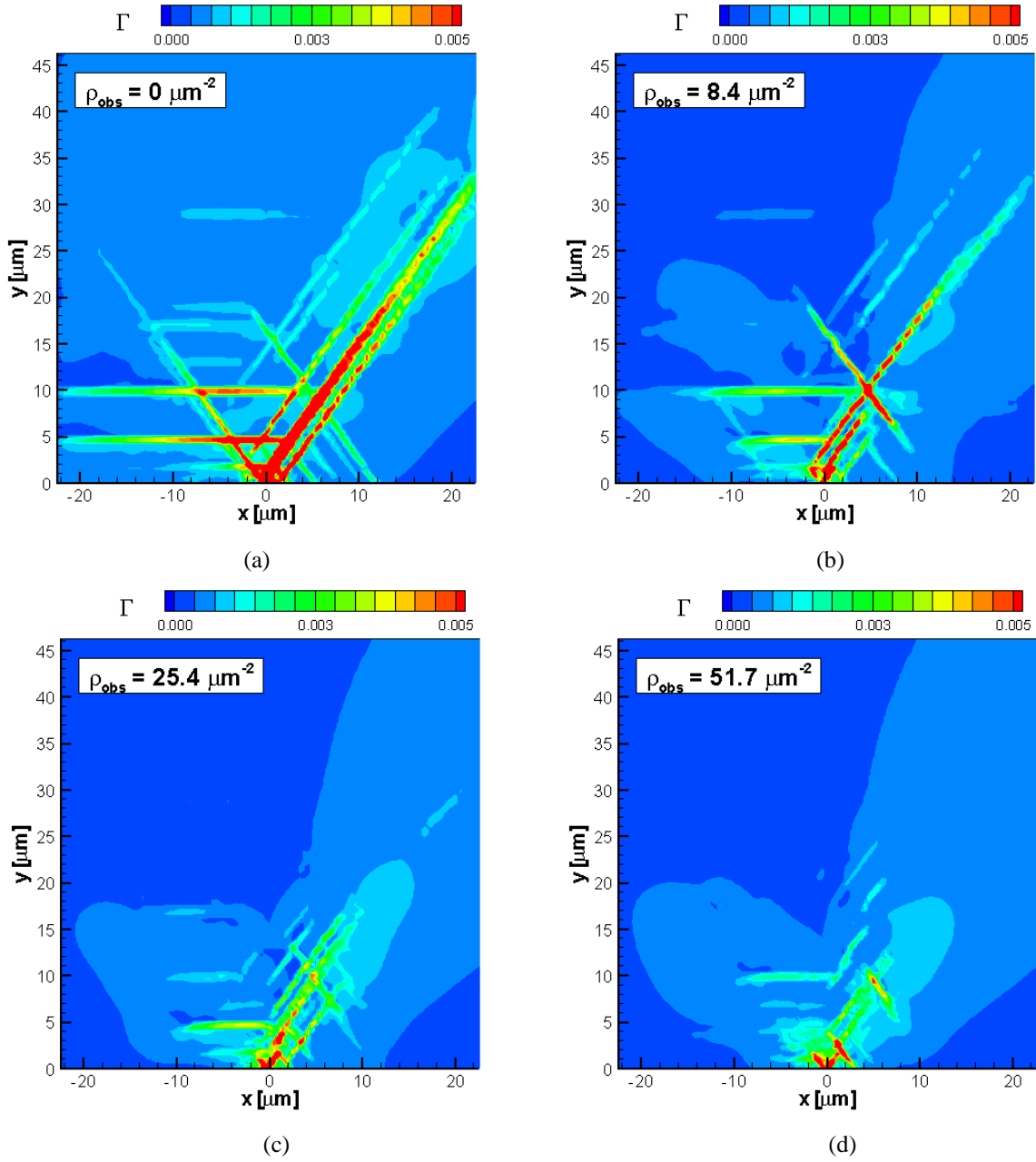
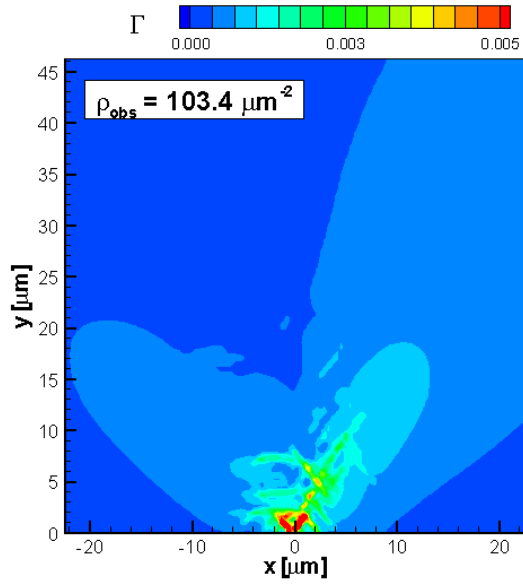
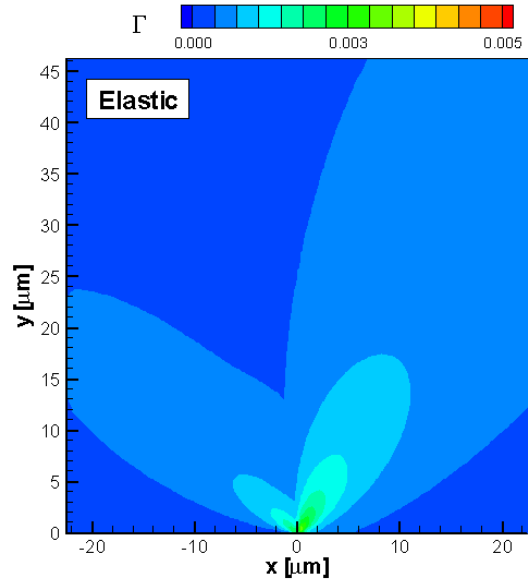


**Figure 6:** Contours of total slip  $\Gamma = \sum |\gamma^{(\alpha)}|$  around the crack tip at  $K_I/K_0 = 0.08$ . (a)  $\rho_{\text{obs}} = 0 \mu\text{m}^{-2}$ , (b)  $\rho_{\text{obs}} = 8.4 \mu\text{m}^{-2}$  (c)  $\rho_{\text{obs}} = 25.4 \mu\text{m}^{-2}$  (d)  $\rho_{\text{obs}} = 51.7 \mu\text{m}^{-2}$  (e)  $\rho_{\text{obs}} = 103.4 \mu\text{m}^{-2}$  (f) Elastic solution.



(e)



(f)

**Figure 6 (cont.):** Contours of total slip  $\Gamma = \sum |\gamma^{(\alpha)}|$  around the crack tip at  $K_I/K_0 = 0.08$ . (a)  $\rho_{obs} = 0 \mu m^{-2}$ , (b)  $\rho_{obs} = 8.4 \mu m^{-2}$  (c)  $\rho_{obs} = 25.4 \mu m^{-2}$  (d)  $\rho_{obs} = 51.7 \mu m^{-2}$  (e)  $\rho_{obs} = 103.4 \mu m^{-2}$  (f) Elastic solution.

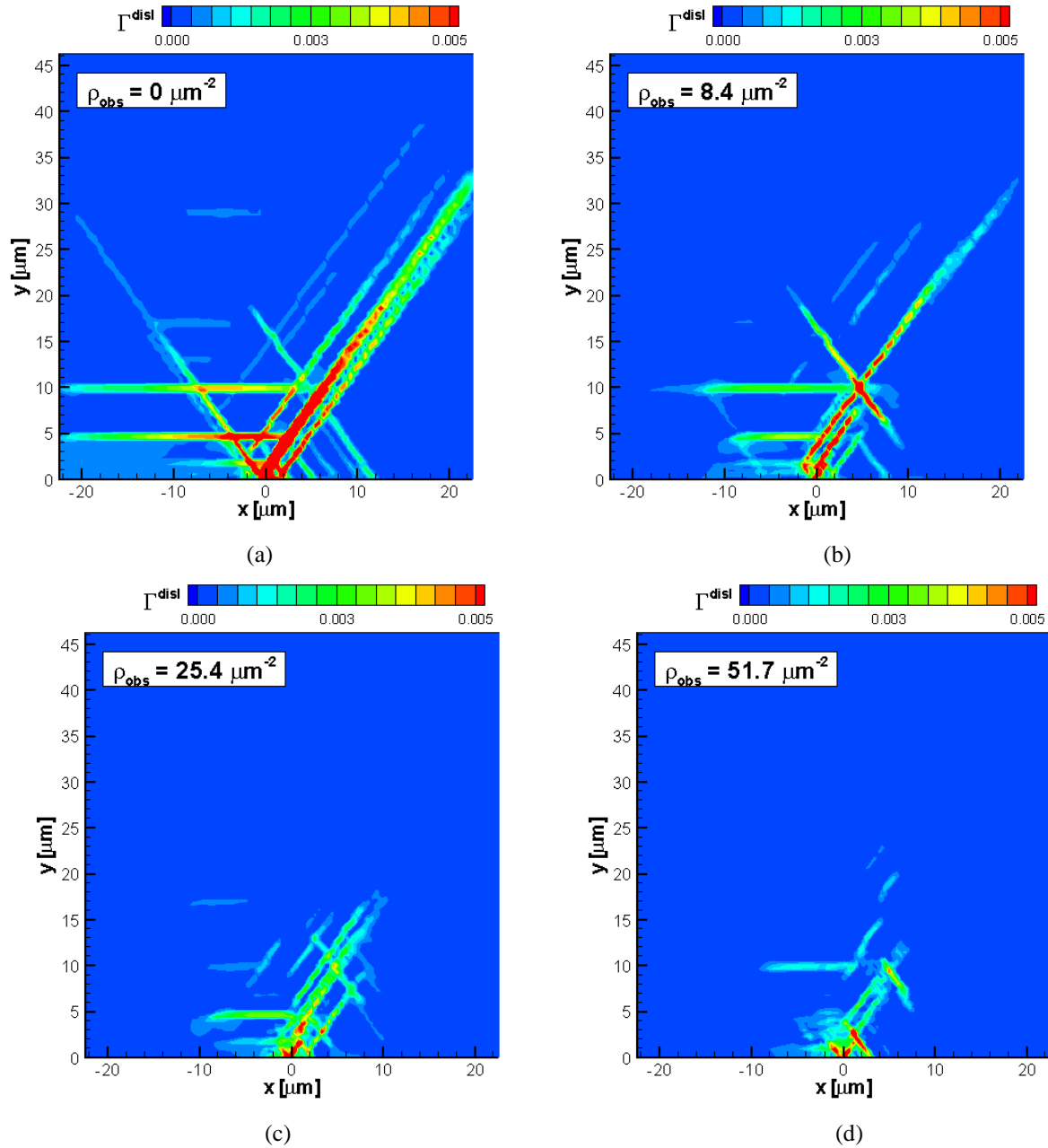


**Figure 7:** Contours of total slip  $\Gamma = \sum |\gamma^{(\alpha)}|$  (contributed only by the dislocations) around the crack tip at  $K_I/K_0 = 0.08$ . (a)  $\rho_{obs} = 0 \mu\text{m}^{-2}$ , (b)  $\rho_{obs} = 8.4 \mu\text{m}^{-2}$  (c)  $\rho_{obs} = 25.4 \mu\text{m}^{-2}$  (d)  $\rho_{obs} = 51.7 \mu\text{m}^{-2}$  (e)  $\rho_{obs} = 103.4 \mu\text{m}^{-2}$  (f) Elastic solution.

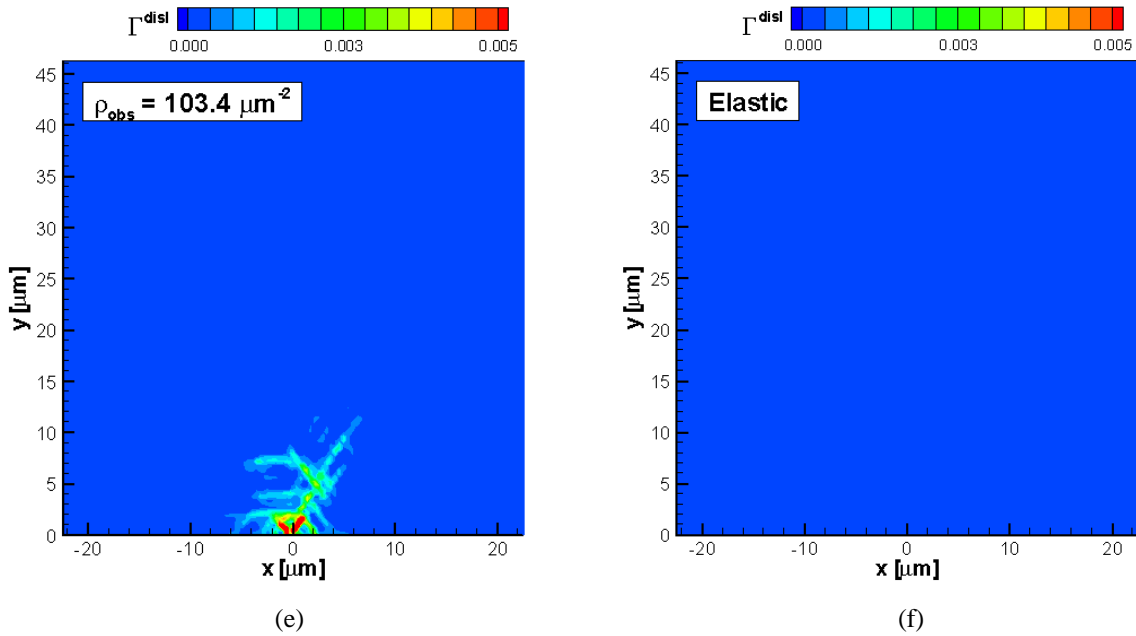


**Figure 7(cont.):** Contours of total slip  $\Gamma = \sum |\gamma^{(\alpha)}|$  (contributed only by the dislocations) around the crack tip at  $K_I/K_0 = 0.08$ . (a)  $\rho_{obs} = 0 \mu\text{m}^{-2}$ , (b)  $\rho_{obs} = 8.4 \mu\text{m}^{-2}$  (c)  $\rho_{obs} = 25.4 \mu\text{m}^{-2}$  (d)  $\rho_{obs} = 51.7 \mu\text{m}^{-2}$  (e)  $\rho_{obs} = 103.4 \mu\text{m}^{-2}$  (f) Elastic solution.

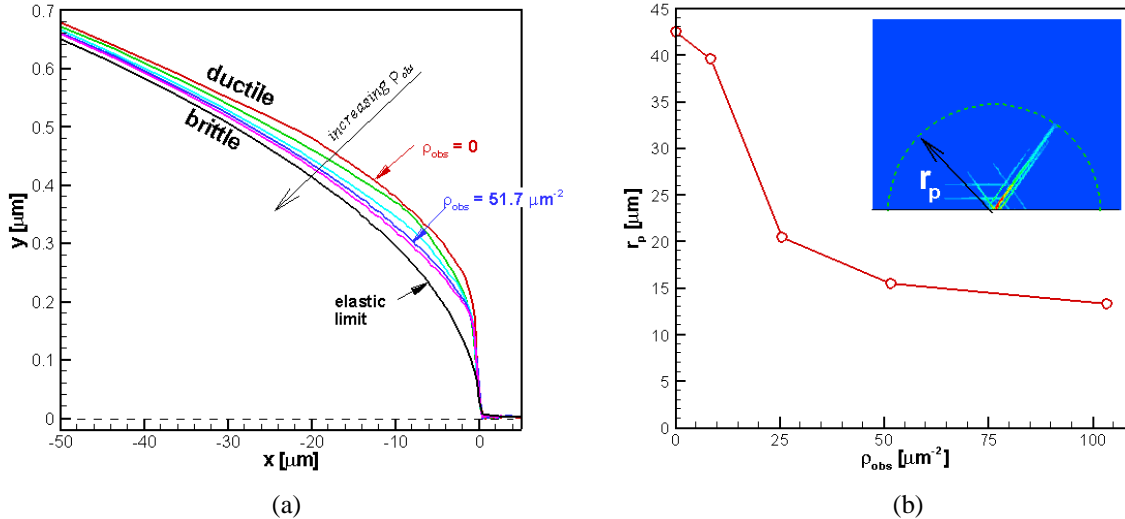


**Figure 8:** (a) Variation of Crack shape at  $K_I/K_0 = 0.08$  with Obstacle Density. (b) Plastic zone size ( $r_p$ ) vs obstacle density at  $K_I/K_0 = 0.08$ .

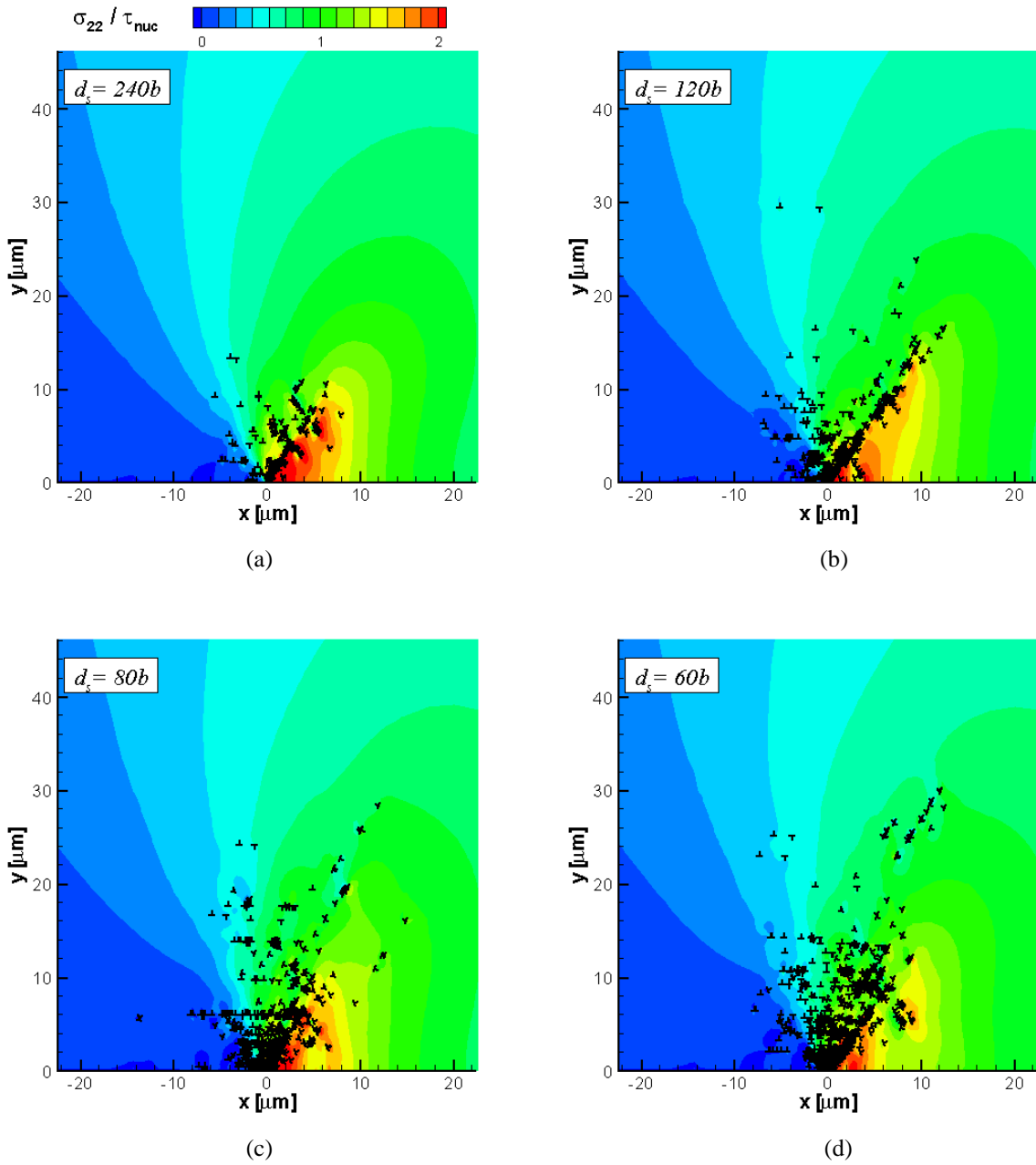


**Figure 9:** Normalized opening stress  $\sigma_{22}/\sigma_{max}$  and dislocation distribution at  $K_I/K_0 = 0.08$  for different slip planes spacing: (a)  $d_s = 240b$ , (b)  $d_s = 120b$ , (c)  $d_s = 80b$ , and (d)  $d_s = 60b$ .

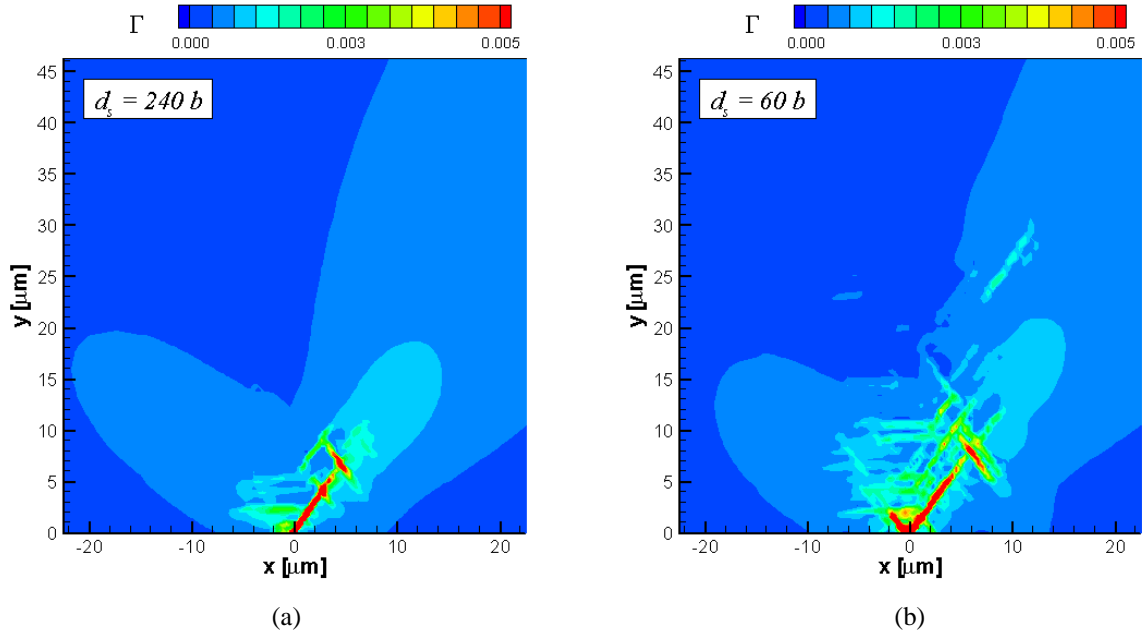


**Figure 10:** Contours of total slip  $\Gamma = \sum |\gamma^{(\alpha)}|$  around the crack tip at  $K_I/K_0 = 0.08$  for two cases with different slip plane spacing: (a)  $d_s = 240b$ , (b)  $d_s = 60b$ .

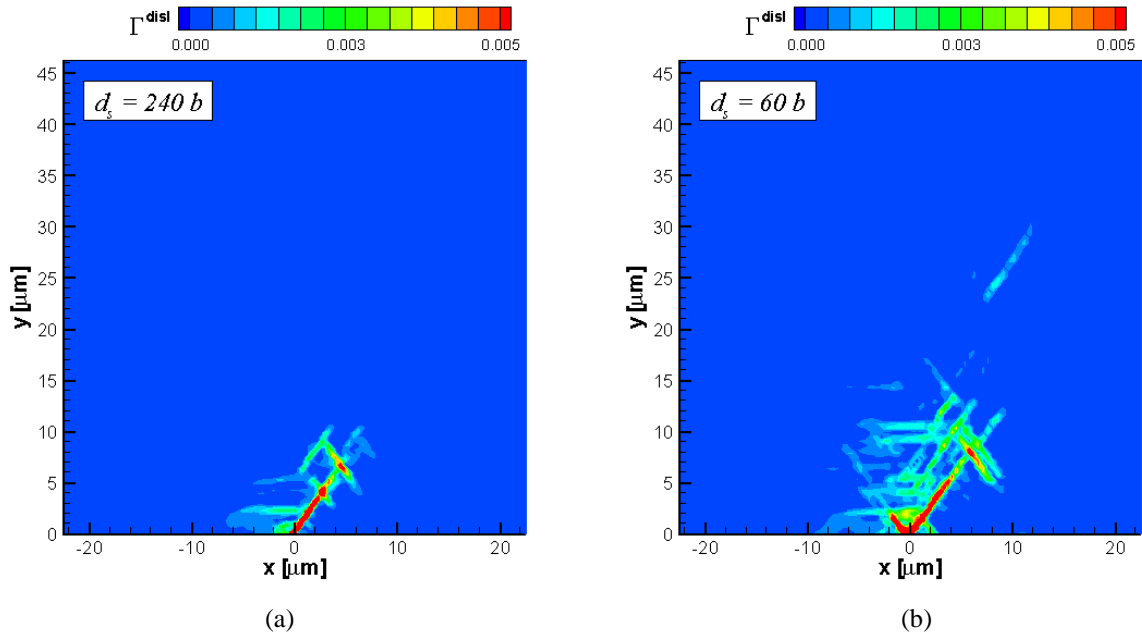


**Figure 11:** Contours of total slip  $\Gamma = \sum |\gamma^{(\alpha)}|$  (contributed only by the dislocations) around the crack tip at  $K_I/K_0 = 0.08$  for two cases with different slip plane spacing: (a)  $d_s = 240b$ , (b)  $d_s = 60b$ . Note the difference in the plastic zone ( $r_p$ ) between the two cases.

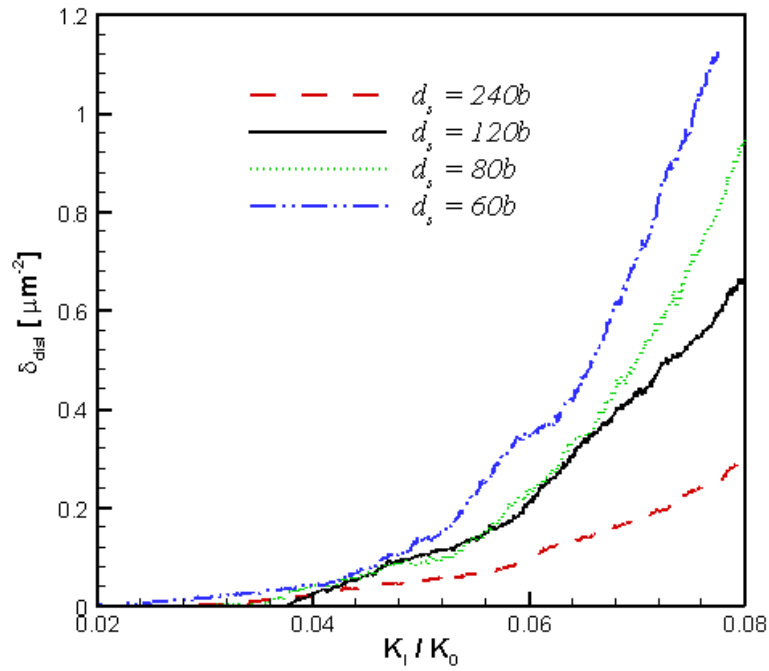


**Figure 12:** Dislocation density measured over the entire process windows versus the normalized applied stress intensity factor  $K_I/K_0$  for the different slip plane spacing for an FCC-like material.

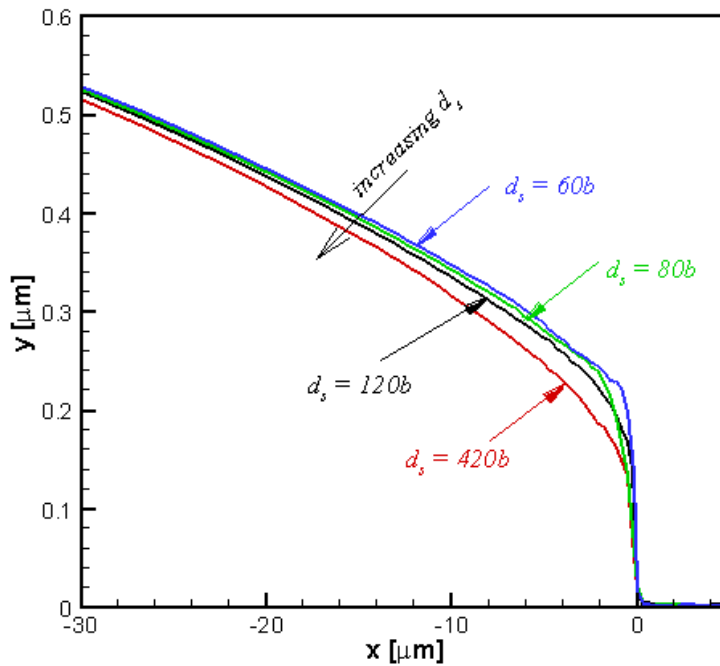


**Figure 13:** Crack shape at  $K_I/K_0 = 0.08$  for different slip plane spacing.

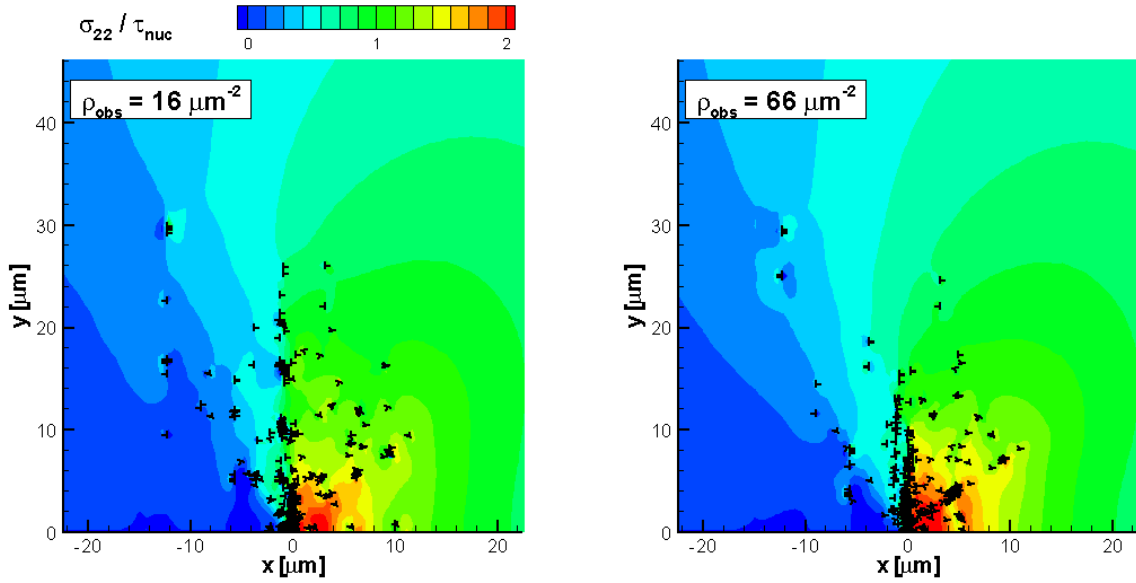


**Figure 14:** Normalized opening stress  $\sigma_{22}/\sigma_{max}$  and dislocation distribution at  $K_I/K_0 = 0.08$  for the bcc-like orientation and two different obstacle densities: (a)  $\rho_{obs} = 16 \mu m^{-2}$ , (b)  $\rho_{obs} = 66 \mu m^{-2}$ .

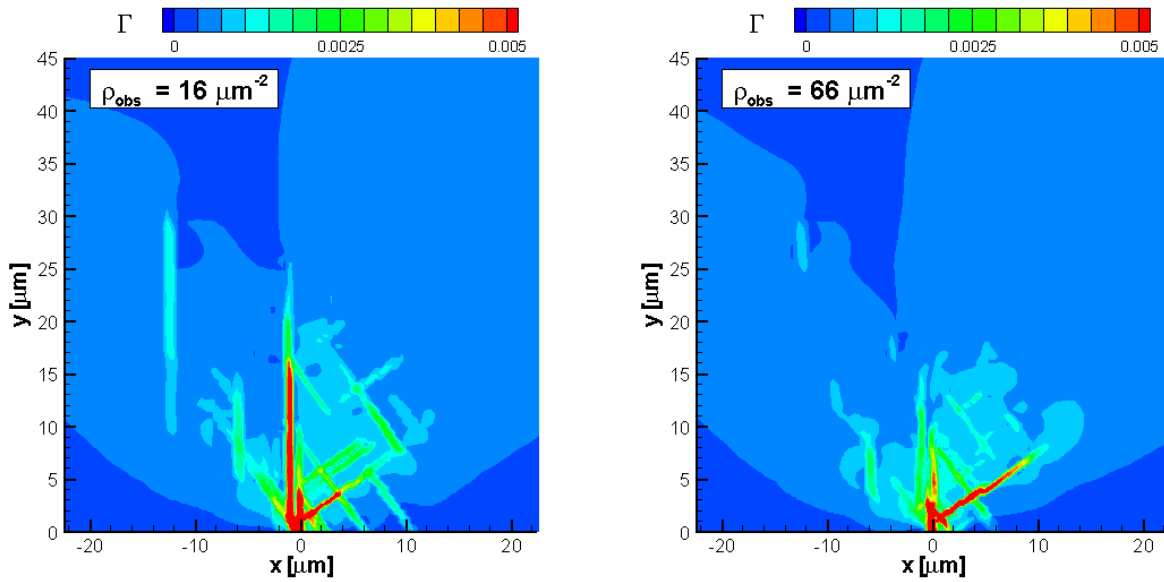


**Figure 15:** Contours of total slip  $\Gamma = \sum |\gamma^{(\alpha)}|$  around the crack tip at  $K_I/K_0 = 0.08$  for the bcc-like orientation and two different obstacle densities: (a)  $\rho_{obs} = 16 \mu m^{-2}$ , (b)  $\rho_{obs} = 66 \mu m^{-2}$ .

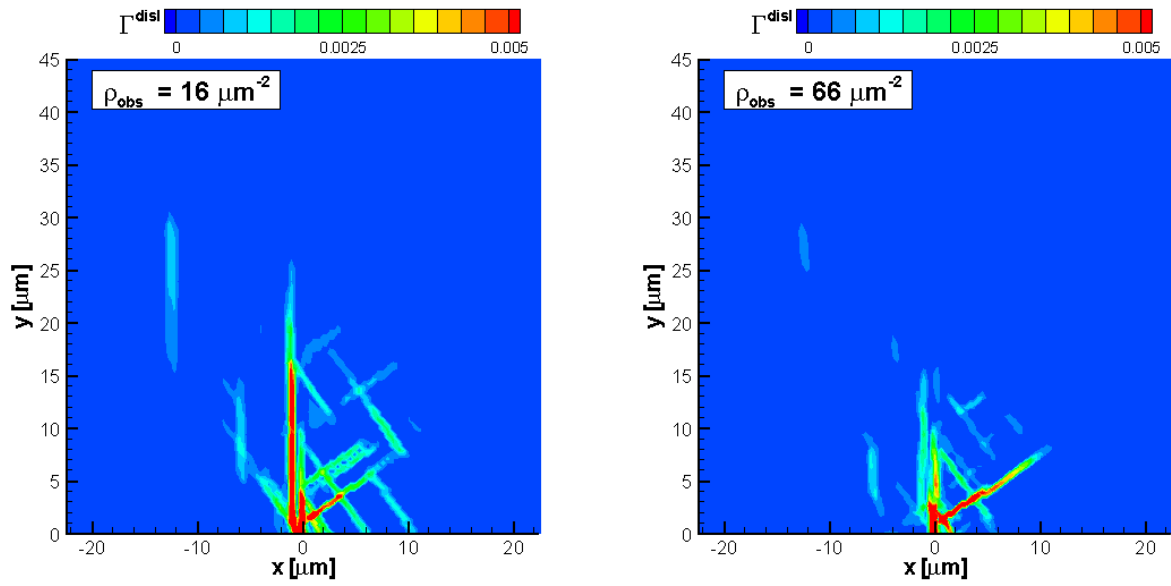


**Figure 16:** Contours of total slip  $\Gamma = \sum |\gamma^{(\alpha)}|$  (contributed only by the dislocations) around the crack tip at  $K_I/K_0 = 0.08$  for the bcc-like orientation and two different obstacle densities: (a)  $\rho_{obs} = 16 \mu\text{m}^{-2}$ , (b)  $\rho_{obs} = 66 \mu\text{m}^{-2}$ .

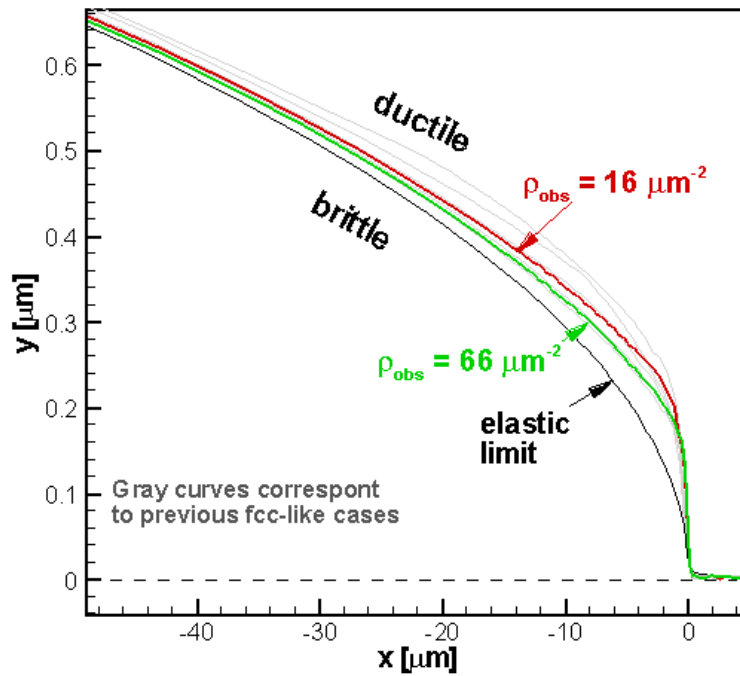


**Figure 17:** Crack shape at  $K_I/K_0 = 0.08$  for the bcc-like orientation and two different obstacle densities.

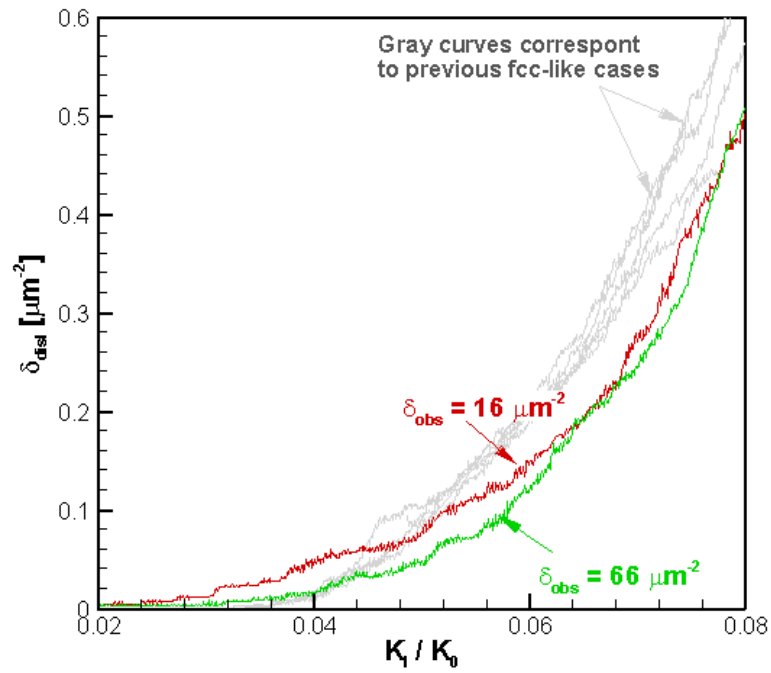


**Figure 18:** Dislocation density measured over the entire process windows versus the normalized applied stress intensity factor  $K_I/K_0$  for the fcc-like (gray) and bcc-like orientations (red and green) with two different obstacle densities.